APPLIED PHYSICS

Ultra-compact broadband polarization diversity orbital angular momentum generator with 3.6 × 3.6 μm² footprint

Nan Zhou[1], Shuang Zheng[1], Xiaoping Cao[1], Yifan Zhao[1], Shengqian Gao[2], Yuntao Zhu[2], Mingbo He[2], Xinlun Cai[2]*, Jian Wang[1]*

Orbital angular momentum (OAM), one fundamental property of light, has been of great interest over the past decades. An ideal OAM generator, fully compatible with existing physical dimensions (wavelength and polarization) of light, would offer the distinct features of broadband, polarization diversity, and ultra-compact footprint. Here, we propose, design, fabricate, and demonstrate an ultra-compact chip-scale broadband polarization diversity OAM generator on a silicon platform with a 3.6 × 3.6 μm² footprint. The silicon OAM chip is formed by introducing a subwavelength surface structure (superposed holographic fork gratings) on top of a silicon waveguide, coupling the in-plane waveguide mode to the out-plane free-space OAM mode. We demonstrate in theory and experiment the broadband generation of polarization diversity OAM modes (x-/y-polarized OAM_{+1}/OAM_{-1}) from 1500 to 1630 nm with high purity and efficiency. The demonstrations of an ultra-compact broadband polarization diversity OAM generator may open up new perspectives for OAM-assisted N-dimensional optical multiplexing communications/interconnects and high-dimensional quantum communication systems.

INTRODUCTION

The spin angular momentum (SAM) of light is one component of angular momentum that is associated with quantum spin and light having circular polarization states. When a light beam is circularly polarized, each of its photons carries an SAM of $\pm\hbar$, where $\hbar$ is the reduced Plank's constant and ± sign is positive for left and negative for right circular polarizations. There is another component of angular momentum, known as orbital angular momentum (OAM) of light, that is dependent on the field spatial distribution but not on the polarization. When a light beam has a helical phase structure $\exp(i\ell\theta)$, as recognized by Allen and co-workers in 1992 (*1*), each of its photons carries an OAM of $\ell\hbar$, where ℓ is the topological charge and θ is the azimuthal angle. The magnitude and sign of ℓ represent the twist rate and twist direction of the helical phase structure. Unlike SAM having only two possible values, OAM, in principle, can take theoretically unbounded values of ℓ. OAM-carrying light has a basic property of "dislocations in wave trains," characterized by phase singularity at the beam center and resultant donut-shaped intensity profile, also called optical vortex, a family of "singular optics." The distinct features of OAM have promoted a variety of applications, including manipulation, trapping, tweezer, imaging, microscopy, sensing, metrology, astronomy, nonlinear interaction, and quantum information processing (*2*–*8*). Very recently, OAM has also seen its potential applications in free-space, fiber-based, and underwater optical communications (*9*–*17*). Traditionally, wavelength and polarization physical dimensions of light have been widely used to increase the transmission capacity by multiplexing multichannel data information. However, these conventional techniques have seen their capacity limit after being fully developed. The space-division multiplexing (SDM) exploiting the spatial structure (the only known physical dimension of light left) provides a promising solution to address the emerging capacity crunch and promises the sustainable increase of aggregate transmission capacity of optical communications (*18*). OAM-carrying spatial modes, forming another mode basis, offer an alternative approach to SDM-enabled optical communications (*9*–*11*).

To enable OAM communications, generating OAM-carrying light beams is of great importance. So far, many techniques have been demonstrated for generating OAM modes, such as laser cavities, mode converters, spatial light modulators (SLMs), spiral phase plates, q-plates, fibers, photonic integrated devices, metamaterials, and metasurfaces (*2*, *19*–*35*). The most convenient way to generate OAM modes is to use the commercially available SLMs (*24*), which, however, are expensive and relatively bulky. In recent years, photonic integrated OAM-carrying optical vortex emitters have been reported (*25*–*32*). Silicon photonics is considered to be an attractive photonic integration platform because of its small footprint for high-density integration, low power consumption, and complementary metal-oxide semiconductor compatibility (*36*). These OAM generation techniques show impressive performance (*19*–*35*). However, most of them have either narrow bandwidth or single-polarization operation or complicated structure with a relatively large footprint. OAM, in physics, is fully compatible with other physical dimensions of light such as wavelength and polarization. The fully combined use of OAM multiplexing technique with already existing well-established multiplexing techniques (wavelength and polarization) is essential to OAM-assisted multidimensional optical communications, that is, the wavelength and polarization properties should be also considered in the design of an OAM generator. In this scenario, a laudable goal would be to develop an ultra-compact broadband polarization diversity OAM generator on a silicon platform.

Here, we propose and demonstrate an ultra-compact broadband polarization diversity photonic integrated OAM generator on a silicon platform. A simple two-dimensional (2D) subwavelength surface structure (superposed holographic fork gratings) is formed on top of the silicon waveguide to couple the in-plane guided mode in the waveguide to the out-plane polarization diversity OAM mode in free space with superior performance (x-pol. OAM_{+1}, x-pol. OAM_{-1}, y-pol.

[1]Wuhan National Laboratory for Optoelectronics, School of Optical and Electronic Information, Huazhong University of Science and Technology, Wuhan, 430074 Hubei, China. [2]State Key Laboratory of Optoelectronic Materials and Technologies and School of Physics and Engineering, Sun Yatsen University, Guangzhou 510275, China.
*Corresponding author. Email: caixlun5@mail.sysu.edu.cn (X.C.); jwang@hust.edu.cn (J.W.)

OAM_{+1}, y-pol. OAM_{-1}). The distinct features of broadband and polarization diversity imply the full compatibility of the ultra-compact footprint OAM generator with existing physical dimensions of light such as wavelength and polarization.

RESULTS

Concept, principle, and theory

The concept and principle of the designed chip-scale broadband polarization diversity OAM generator on a silicon platform are illustrated in Fig. 1, in which the incident fundamental mode (TE_0) from four ports (in-plane guided mode) is coupled into the polarization diversity free-space OAM mode (out-plane vertically emitted mode) by the 2D subwavelength surface structure (superposed holographic fork gratings). The zoom-in superposed holographic fork grating region is shown in Fig. 1A. The formation, principle, and theory of the surface grating on top of the silicon waveguide rely on the holographic method (*37*, *38*), which could be briefly explained as follows.

The target OAM mode, having a 3D spiral phase structure (e.g., y-pol. OAM_{+1} in Fig. 1C), is vertically incident to the waveguide surface. Meanwhile, there is also an in-plane guided mode (e.g., y-pol. TE_0 along x direction) propagating from left to right in the waveguide (Fig. 1C). The target OAM mode and the in-plane guided mode are expressed as

$$E_{\mathrm{OAM}} = A\exp(i\ell\theta) \tag{1}$$

$$E_{\mathrm{waveguide}} = B\exp(ikx) \tag{2}$$

where A and B are amplitudes of the target OAM mode and the in-plane guided mode, respectively. ℓ is the topological charge or order of OAM mode (ℓ = +1 in Fig. 1C), and θ is the azimuthal angle. k is the propagation constant of the silicon waveguide mode. The azimuthal angle θ in polar coordinates is related to the Cartesian coordinates by $\tan\theta = y/x$. The coupled interference between the vertically incident OAM mode and the in-plane

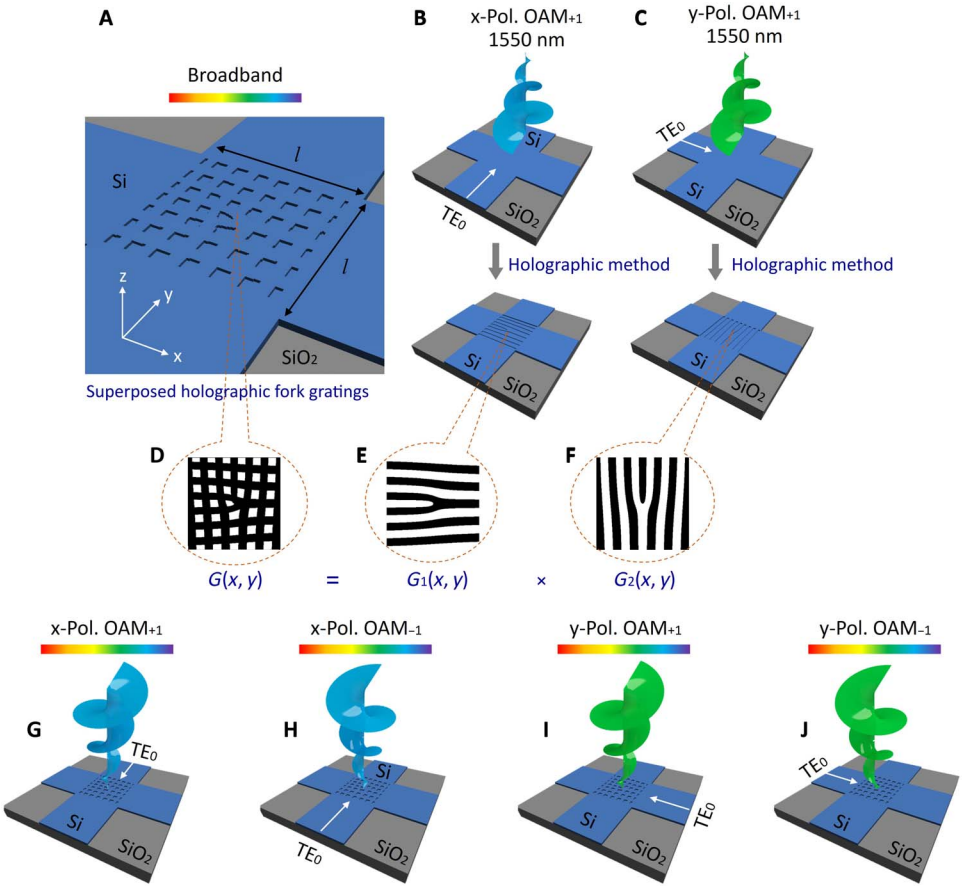

Fig. 1. Concept and principle of chip-scale broadband polarization diversity OAM generator on a silicon platform. (**A**) Zoom-in 2D subwavelength surface structure (superposed holographic fork gratings) region. (**B** and **C**) Illustration of holographic method producing fork gratings. The coupled interference between the vertically incident x-pol. (B) or y-pol. (C) OAM mode and the x-pol. (B) or y-pol. (C) TE_0 in-plane guided mode forms a fork grating on top of the silicon waveguide with the fork opening direction along x (B) or y (C). (**D** to **F**) Superposed holographic fork gratings $G(x, y)$ (D) formed by the superposition of two fork gratings of $G_1(x, y)$ with the fork opening direction along x (E) and $G_2(x, y)$ with the fork opening direction along y (F). (D) to (F) correspond to (A) to (C), respectively. (**G** to **J**) Superposed holographic fork gratings for generating broadband polarization diversity x-pol. OAM_{+1} (G), x-pol. OAM_{-1} (H), y-pol. OAM_{+1} (I), and y-pol. OAM_{-1} (J) under different incident conditions of −y-input x-pol. (G), y-input x-pol. (H), −x-input y-pol. (I), and x-input y-pol. (J) TE_0 in-plane waveguide mode. x-Pol., x-polarization; y-Pol., y-polarization.

guided mode forms a fork grating (fork opening direction: y) on top of the silicon waveguide ($z = 0$) (Fig. 1C). The distribution of the fork grating is written by

$$\begin{aligned}\text{Hologram}_{\text{fork}} &= |E_{\text{OAM}} + E_{\text{waveguide}}|^2 \\ &= |A\exp(i\ell\theta) + B\exp(ikx)|^2 \\ &= A^2 + B^2 + AB\exp(-i\ell\theta)\cdot\exp(ikx) + \\ &\quad AB\exp(i\ell\theta)\cdot\exp(-ikx) \\ &= A^2 + B^2 + 2AB\cos(kx - \ell\theta)\end{aligned} \tag{3}$$

The fork grating is transferred onto the silicon waveguide. The amplitude grating in Eq. 3 is converted into a binary phase hologram based on the current fabrication technique expressed as

$$\text{Hologram}_{\text{biphase}} = T\cdot\exp\{i[A^2 + B^2 + 2AB\cdot\text{binary}(\cos(kx - \ell\theta))]\} \tag{4}$$

where T denotes the transmission coefficient of the binary phase hologram.

$$\text{Binary}\big(\cos(kx - \ell\theta)\big) = \begin{cases} 1, & -\pi/2 + 2n\pi \le kx - \ell\theta < \pi/2 + 2n\pi \\ -1, & \pi/2 + 2n\pi \le kx - \ell\theta < 3\pi/2 + 2n\pi \end{cases}, \quad n = 0, \pm1, \pm2, \ldots.$$

The periodic function of Eq. 4 can be expanded into Fourier series written by

$$\text{Hologram}_{\text{biphase}} = \sum_{m=-\infty}^{m=\infty} F_m \exp[im(kx - \ell\theta)] \tag{5}$$

where

$$F_0 = T\cdot\exp[i(A^2 + B^2)]\cdot\cos(2AB) \tag{6}$$

$$F_m = \begin{cases} 2T\cdot(-1)^{\frac{m-1}{2}}/ & , \quad m \text{ is odd number} \\ (m\pi)\cdot i\exp[i(A^2 + B^2)]\cdot\sin(2AB) & \\ 0 & , \quad m \text{ is even number} \end{cases} \tag{7}$$

where $A^2 + B^2$ is the bias phase retardation and $2AB$ is the amplitude of the phase modulation.

When the binary phase hologram is illuminated with the same in-plane guided mode (e.g., y-pol. TE_0 along x direction) propagating from left to right in the waveguide [$E_{\text{left}} = B\exp(ikx)$], the output field ($E_{\text{out1}} = E_{\text{left}} \cdot \text{Hologram}_{\text{biphase}}$) contains a term of the form

$$E_{\text{OAM1}}^{\text{y-pol}} = -C\exp(i\ell\theta) \tag{8}$$

where $C = T\cdot\exp[i(A^2 + B^2)]\cdot(2/\pi)\cdot\sin(2AB)$. $E_{\text{OAM1}}^{\text{y-pol}}$, independent of kx, represents an OAM beam having vertical emission. When observing the output field term $E_{\text{OAM1}}^{\text{y-pol}}$ above the silicon waveguide, the topological charge value of the OAM beam is reversed [$\exp(i\ell\theta) \rightarrow \exp(-i\ell\theta)$] (e.g., y-pol. OAM_{-1}).

When the binary phase hologram is illuminated with the opposite in-plane guided mode (e.g., y-pol. TE_0 along $-x$ direction) propagating from right to left in the waveguide [$E_{\text{right}} = B\exp(-ikx)$], owing to the similar principle of holography, the output field ($E_{\text{out2}} = E_{\text{right}} \cdot \text{Hologram}_{\text{biphase}}$) contains a term of the form

$$E_{\text{OAM2}}^{\text{y-pol}} = C\exp(-i\ell\theta) \tag{9}$$

$E_{\text{OAM2}}^{\text{y-pol}}$ also represents an OAM beam. Note that, when observing the output field term $E_{\text{OAM2}}^{\text{y-pol}}$ above the silicon waveguide, the topological charge value of the OAM beam is reversed [$\exp(-i\ell\theta) \rightarrow \exp(i\ell\theta)$] (e.g., y-pol. OAM_{+1}). Hence, the output OAM beam has an opposite topological charge value ($-\ell$,ℓ) for incident light from left to right and from right to left.

Similarly, for another fork grating (fork opening direction: x) formed by the coupled interference between the vertically incident OAM mode (e.g., x-pol. OAM_{+1}) and the in-plane guided mode (e.g., x-pol. TE_0 along y direction) propagating from bottom to top in the waveguide (Fig. 1B), x-pol. OAM_{-1} and x-pol. OAM_{+1} with vertical emission can be achieved when illuminated with incident light from bottom to top and from top to bottom.

Superposed holographic fork gratings [$G(x, y)$] on top of the silicon waveguide are then formed by the superposition of two fork gratings [$G_1(x, y)$ and $G_2(x, y)$] with fork opening directions along x and y, respectively (Fig. 1, D to F). Consequently, a polarization diversity OAM generator (x-pol. OAM_{+1}, x-pol. OAM_{-1}, y-pol. OAM_{+1}, y-pol. OAM_{-1}) is realized when using superposed holographic fork gratings on top of the silicon waveguide under different incident conditions of –y-input x-pol., y-input x-pol., –x-input y-pol., and x-input y-pol. TE_0 in-plane guided mode (Fig. 1, G to J).

Design and simulations

In the structure design, the coupled interference region is divided into many pixels (pixel size: 100 nm × 100 nm), with each pixel set by a value of $g(x, y)$. A simple binary function of $g(x, y)$ is considered according to the binary phase hologram in Eq. 4. The two phase values of each pixel in the binary phase hologram are mapped to the Si and SiO_2, respectively. Hence, the derived binary phase hologram is transferred to a subwavelength surface structure on top of the silicon waveguide. The amplitude of the phase modulation in the binary phase hologram is dependent on the etching depth of the silicon waveguide.

To provide a theoretical basis for the device fabrication, we verify the designed OAM generator by numerical simulations based on the 3D finite-difference time-domain (3D-FDTD) method. The far field is calculated by the scalar diffraction theory. The geometry of the superposed holographic fork grating region is a square with a length of l (the same as the waveguide width). The silicon in the grating region is etched by a depth of h and covered by the upper SiO_2 cladding. We simulate the designed OAM generator and evaluate the purity and scattering efficiency (see Materials and Methods) of the generated polarization diversity OAM modes. Note that the purity and scattering efficiency of the generated OAM modes are dependent on the geometric parameters (e.g., length l of the grating region and etching depth h). The proper optimization of the geometric parameters can enable a high-quality chip-scale OAM generator.

To ensure the calculation accuracy, we study the purity (y-pol. OAM_{+1} as one example) as a function of the mesh size used in the 3D-FDTD simulations. As shown in Fig. 2A, one can see that the calculated purity becomes almost constant as the mesh size is smaller than 70 nm. In the simulations, we use an even smaller mesh size of 40 nm. Hence, it is believed that the accuracy of the simulation results can be guaranteed.

We study the purity of the generated polarization diversity OAM modes (x-pol. OAM_{+1}, x-pol. OAM_{-1}, y-pol. OAM_{+1}, y-pol. OAM_{-1}) as a function of the length l of the grating region (2 to 10 μm). The etching depth is 60 nm. As shown in Fig. 2B, the average purity shows a maximum value of 0.91 when l = 3.6 μm, which is selected as the optimized geometric parameter for the device fabrication. The minimum average purity is ~0.83 (length l: 2 μm). When the length l is 10 μm, the average purity is ~0.84. For l = 3.6 μm, the purity of x-pol. OAM_{+1}, x-pol. OAM_{-1}, y-pol. OAM_{+1}, and y-pol. OAM_{-1} is 0.908, 0.901, 0.915, and 0.914, respectively. They are also the corresponding maximum purity of each OAM mode when varying the length l of the grating region from 2 to 10 μm. This phenomenon could be briefly explained as follows. According to the theory of the holographic method in Eq. 4, holographic fork grating region is dependent on the propagation constant k of the silicon waveguide mode. Note that the propagation constant k of the silicon waveguide mode is related to the mode effective refractive index, which is dependent on the geometric parameter (e.g., length l of the grating region). For a given design of the fork grating, there might exist an optimal length l of the grating region fitting well to the designed grating and giving the maximum purity of the generated OAM modes.

We study the purity of the generated polarization diversity OAM modes (x-pol. OAM_{+1}, x-pol. OAM_{-1}, y-pol. OAM_{+1}, y-pol. OAM_{-1}) as a function of the depth h. The length l is 3.6 μm. As shown in Fig. 2C, the purity changes slightly as the depth h is less than 120 nm. When the depth h is larger than 120 nm, the purity drops with the increase of the depth h.

We study the purity of the generated polarization diversity OAM modes (x-pol. OAM_{+1}, x-pol. OAM_{-1}, y-pol. OAM_{+1}, y-pol. OAM_{-1}) as a function of the wavelength. The length l is 3.6 μm and the depth h is

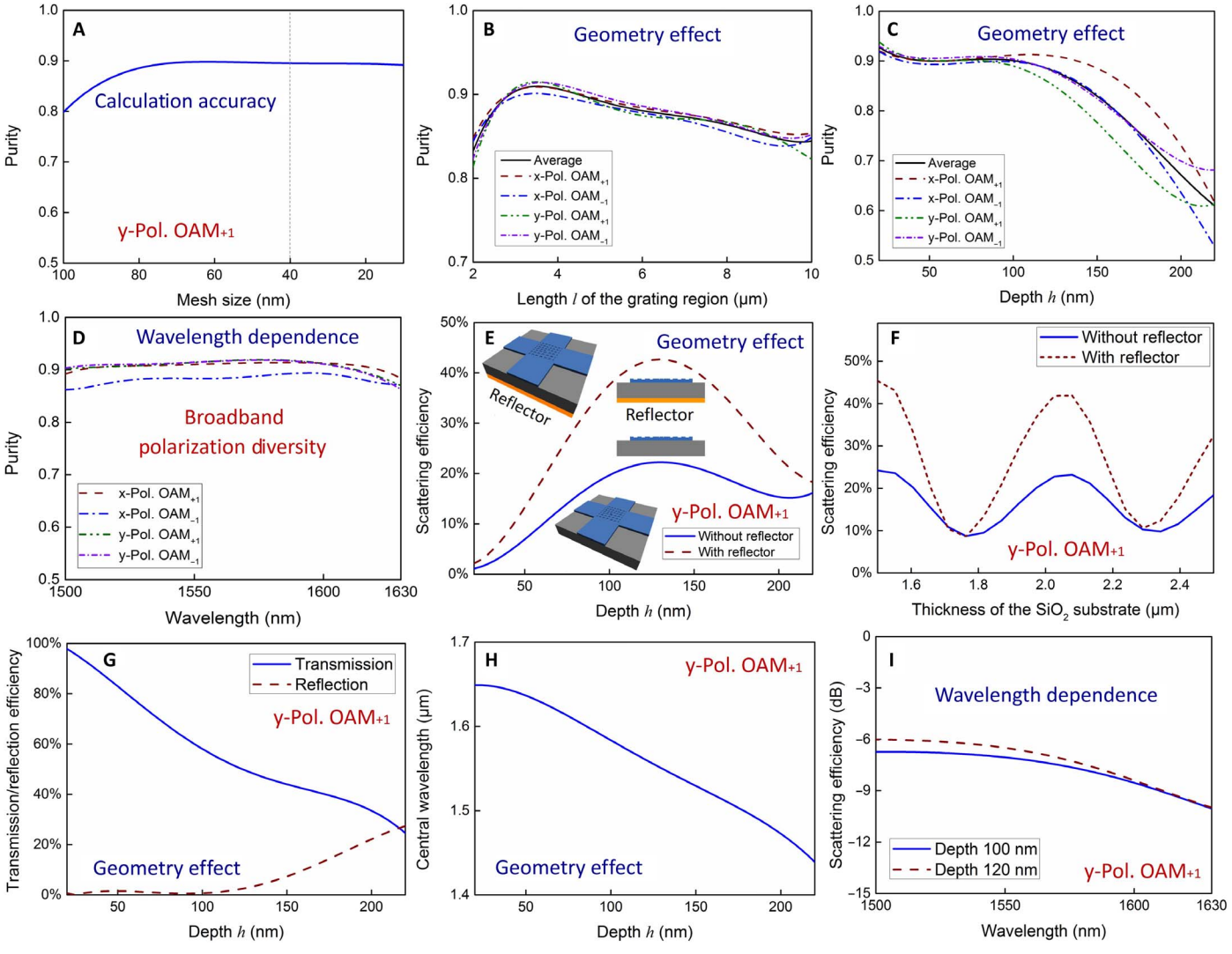

Fig. 2. Simulation results for characterizing the polarization diversity OAM generator. (**A**) Purity (y-pol. OAM_{+1}) versus mesh size used in the 3D-FDTD simulations (length l: 3.6 μm; depth h: 60 nm). (**B**) Purity of polarization diversity OAM modes versus length l of the grating region (depth h: 60 nm). (**C**) Purity of polarization diversity OAM modes versus depth h (length l: 3.6 μm). (**D**) Purity of polarization diversity OAM modes versus wavelength (length l: 3.6 μm; depth h: 60 nm). (**E**) Scattering efficiency (y-pol. OAM_{+1}) without and with a reflector versus depth h (length l: 3.6 μm). (**F**) Scattering efficiency (y-pol. OAM_{+1}) without and with a reflector versus thickness of the SiO_2 substrate (length l: 3.6 μm; depth h: 120 nm). (**G**) Transmission/reflection efficiency versus depth h (length l: 3.6 μm). (**H**) Central wavelength versus depth h (length l: 3.6 μm). (**I**) Scattering efficiency versus wavelength at two depths of 100 and 120 nm (length l: 3.6 μm).

60 nm. The designed chip-scale polarization diversity OAM generator relying on the subwavelength surface structure shows broadband property. As shown in Fig. 2D, the maximum purity of x-pol. OAM_{+1} mode is 0.91. With the wavelength varying from 1507 to 1621 nm, the purity of x-pol. OAM_{+1} mode is larger than 0.9. For x-pol. OAM_{-1} mode, the maximum purity is 0.89. When changing the wavelength from 1525 to 1616 nm, the purity of x-pol. OAM_{-1} mode is larger than 0.88. For y-pol. OAM_{+1} mode, the maximum purity is 0.92. In the wavelength range from 1500 to 1612 nm, the purity of y-pol. OAM_{+1} mode is larger than 0.9. For y-pol. OAM_{-1} mode, the maximum purity is 0.92. Within a wavelength range from 1500 to 1610 nm, the purity of y-pol. OAM_{-1} mode is larger than 0.9. Hence, the designed polarization diversity OAM generator has a bandwidth of 114 nm (purity: >90%) for x-pol. OAM_{+1}, 91 nm (purity: >88%) for x-pol. OAM_{-1}, 112 nm (purity: >90%) for y-pol. OAM_{+1}, and 110 nm (purity: >90%) for y-pol. OAM_{-1}.

We study the scattering efficiency of the generated OAM mode (y-pol. OAM_{+1} as one example) as a function of the depth h. The length l is 3.6 μm. As shown in Fig. 2E, one can see that the maximum scattering efficiency is about 22.3%. At the etching depth of 100 and 120 nm, the simulated scattering efficiency is about 19.8 and 22.0%, respectively. Since a portion of light is emitted downward, which enters into the substrate and induces loss, one potential way to improve the scattering efficiency is to add a reflection layer (*39*). We simulate the improved design by adding a thin gold film under the SiO_2 substrate. The thickness of the gold film is 100 nm. As shown in Fig. 2E, by adding a gold film reflector, the maximum scattering efficiency of the y-pol. OAM_{+1} is about 43%, which is almost twice the efficiency without the reflection layer. Insets of Fig. 2E also illustrate the 3D structure and cross-sectional view of the device without and with the reflection layer. Hence, adding a reflection layer could be an efficient way to improve the scattering efficiency of the generated OAM modes.

When adding a gold film reflector under the SiO_2 substrate to increase the scattering efficiency, the output OAM mode consists of two parts, one directly coupled from the in-plane guided mode, while the other from the reflected wave by the reflector. The efficiency of the grating is dependent on the thickness of the SiO_2 substrate due to destructive and constructive interference between the reflected wave and directly coupled wave. Actually, the reflected wave also exists even without a gold film reflector. We study the scattering efficiency of the generated OAM mode (y-pol. OAM_{+1} as one example) as a function of the thickness of the SiO_2 substrate. The length l is 3.6 μm and the depth h is 60 nm. Structures without and with a gold film reflector are both considered for comparison. As shown in Fig. 2F, no matter adding a reflector or not, the scattering efficiency depends periodically on the SiO_2 thickness and reaches its maximum with a SiO_2 thickness of around 2.05 μm. For the silicon-on-insulator wafer used in the device fabrication with a SiO_2 thickness of 2 μm, the reflected wave and directly coupled wave have almost identical phase (approximately multiple of 2π), leading to near constructive interference (in-phase) and maximum output OAM mode. One can see from Fig. 2F that adding a gold film reflector can effectively increase the scatter efficiency of the OAM mode generation.

We also simulate the transmitted light through the grating region as a function of the depth h. The length l is 3.6 μm. As shown in Fig. 2G, the transmitted power through the grating region decreases with the increase of the etching depth. Hence, a relatively large depth benefits less transmitted light through the grating region. Moreover, the reflected light by the fork grating region is also simulated as shown in Fig. 2G.

We study the central wavelength as a function of the depth h. The length l is 3.6 μm. Here, the central wavelength means the wavelength at which the incident in-plane guided mode has its propagation constant k related term [e.g., $\exp(ikx)$ or $\exp(-ikx)$] perfectly cancelled by the fork grating (vertical emission of the generated OAM mode). For a given design of the fork grating (optimized for a specific depth h), when changing the depth h, the effective index of the in-plane guided mode also changes, and therefore, the central wavelength is also changed. As shown in Fig. 2H, the central wavelength of the grating is designed at 1550 nm when the depth h is 120 nm. One can see from Fig. 2H that the central wavelength decreases with the increase of the depth h. Although the central wavelength is dependent on the depth h, for a fabricated device with a given depth h, broadband properties in terms of scattering efficiency and purity are still achievable.

We also study the scattering efficiency (y-pol. OAM_{+1} as one example) as a function of the wavelength at two depths of 100 and 120 nm. The length l is 3.6 μm. As shown in Fig. 2I, one can see the broadband generation of OAM mode with favorable scattering efficiency. By varying the wavelength from 1500 to 1630 nm, the scattering efficiency slightly changes from −6.7 to −9.9 dB for depth h = 100 nm and from −6 to −10 dB for depth h = 120 nm. On the basis of the detailed simulation results shown in Fig. 2, one can see that there exist optimized geometric parameters (length l: 3.6 μm; depth h: 100 to 130 nm) to achieve relatively high purity and scattering efficiency.

Figure 3 (A to D) shows detailed simulation results for the generation of four polarization diversity OAM modes (x-pol. OAM_{+1}, x-pol. OAM_{-1}, y-pol. OAM_{+1}, y-pol. OAM_{-1}) without a reflector in the optical communication band (C-band), respectively. The first, second, and third columns in Fig. 3 (A to D) correspond to the intensity profile (square of the amplitude), phase distribution, and interferogram, respectively. The interferogram is obtained via the interference between the generated OAM mode and a reference Gaussian beam with the same polarization. One can see the donut-shaped intensity profile and spiral phase distribution for the generated OAM modes. One can also confirm the order (magnitude and sign) of the generated OAM modes from the number of twists and twist direction in the interferograms. The simulation results of intensity profile, phase distribution, and interferogram with almost identical performance in the C-band are in agreement with the broadband property as shown in Fig. 2D.

To display the evolution process of in-plane guided mode to out-plane OAM mode, we use the 3D-FDTD method to simulate the electrical field distributions along the waveguide and at different height of the fork grating region (z = 0, bottom of the silicon layer) without a reflector. The simulated amplitude distributions of the electric field components are shown in Fig. 3 (E to H). The real part distributions of the electric field components are shown in fig. S1. As shown in Fig. 3 (E to H), one can see how the incident in-plane guided mode gradually evolves when propagating from the traveling waveguide region to the superposed holographic fork grating region and eventually emits from the grating region and becomes out-plane OAM mode in free space with donut-shaped amplitude distribution at the far field. One can also see from Fig. 3 that polarization diversity OAM mode generation (x-pol. OAM_{+1}, x-pol. OAM_{-1}, y-pol. OAM_{+1}, y-pol. OAM_{-1}) is realized under different incident conditions.

We also use the 3D-FDTD method to simulate the generation of polarization diversity OAM modes when adding a gold film reflector to the structure. As shown in Fig. 3 (I to L), one can see the successful generation of polarization diversity OAM modes (x-pol. OAM_{+1}, x-pol. OAM_{-1}, y-pol. OAM_{+1}, y-pol. OAM_{-1}) with a reflector. Compared to

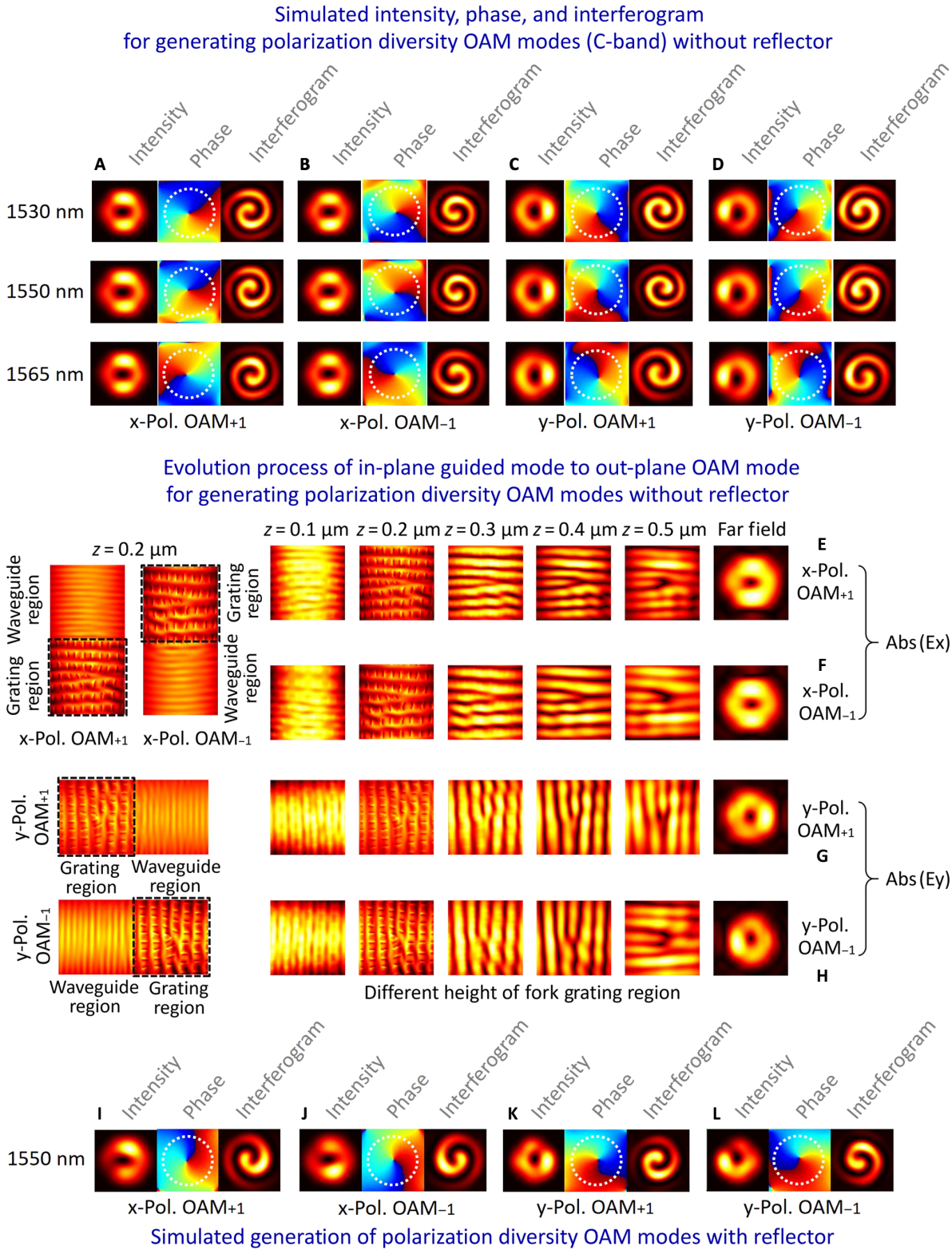

Fig. 3. Simulation results for the generation of polarization diversity OAM modes and the evolution process of in-plane guided mode to out-plane OAM mode. (**A** to **D**) Intensity profile, phase distribution, and interferogram of the generated polarization diversity OAM modes without a reflector in the C-band (1530 to 1565 nm). (**E** to **H**) Electric field distributions (amplitude of electric field components) along the waveguide (from waveguide region to grating region) and at different height of the grating region (z = 0.1, 0.2, 0.3, 0.4, 0.5 μm, far field) without a reflector. (A and E) x-pol. OAM_{+1}. (B and F) x-pol. OAM_{-1}. (C and G) y-pol. OAM_{+1}. (D and H) y-pol. OAM_{-1}. (**I** to **L**) Intensity profile, phase distribution, and interferogram of the generated polarization diversity OAM modes with a reflector at 1550 nm. (I) x-pol. OAM_{+1}. (J) x-pol. OAM_{-1}. (K) y-pol. OAM_{+1}. (L) y-pol. OAM_{-1}. (A to L) Length l: 3.6 μm. (A to D) Depth h: 60 nm. (E to H) Depth h: 100 nm. (I to L) Depth h: 120 nm.

the simulated intensity profile, phase distribution, and interferogram for generating polarization diversity OAM modes without a reflector (Fig. 3, A to D), one can see similar mode quality of the generated polarization diversity OAM modes with negligible performance degradation when adding a gold film reflector to the structure. Thus, the reflected wave by the gold film reflector does not break the integrity of the spatial structure of the output OAM mode, which is beneficial from the parallel structure of the silicon layer, SiO_2 substrate, and gold film reflector. The output OAM mode consists of two parts, i.e., directly coupled wave and reflected wave. The reflected wave suffers a relative delay with respect to the directly coupled wave. The relative delay can be expressed as $\Delta t = 2n_{SiO2}d/c$, where n_{SiO2} and d are the refractive index and thickness (2 μm) of the SiO_2 substrate, respectively, and c is the light velocity in vaccum. The relative delay Δt is estimated to be ~19.2 fs. When modulating data signal onto the incident in-plane guided mode, the estimated relative delay Δt = ~19.2 fs between the reflected wave and directly coupled wave is negligible and far smaller than the symbol period of widely used data rate signal such as 10 Gbit/s (100 ps), 40 Gbit/s (25 ps), and even 100 Gbit/s (10 ps). As a result, the relatively delayed reflected wave has a negligible effect on the signal quality even for practical data signal carrying optical communications applications.

Device fabrication

On the basis of the structure design, theories, and simulation results, we fabricate a chip-scale polarization diversity OAM generator on a silicon platform with different device geometric parameters (length l: 2.4, 3.6, 5, and 10 μm; depth h: 60, 100, and 120 nm). The details of the device fabrication process are shown in fig. S2. Figure 4 (A to D) shows the measured optical microscope and scanning electron microscopy (SEM) images of the fabricated silicon OAM generator (length l: 3.6 μm; depth h: 60 nm). In Fig. 4A, the layout of superposed holographic fork gratings connected by four adiabatic tapers for polarization diversity OAM generation is shown. In Fig. 4B, the SEM image of the superposed holographic fork grating region, which has an ultra-compact footprint of 3.6 × 3.6 μm^2, is shown. One can see the 2D subwavelength surface structure formed on top of the silicon waveguide. In Fig. 4C, the measured optical microscope image of the device is shown. No light is emitted from the device without incidence of the in-plane guided mode. For comparison, the measured near-field view for generating y-pol. OAM_{-1} is shown in Fig. 4D with the incidence of in-plane guided mode. One can observe the bright spot in the grating region, which is the near-field distribution of the emitted OAM mode from the center fork grating region. Figure 4 (E to H) shows the measured optical microscope images of the fabricated silicon OAM generators with different lengths l of the grating region (length l: 2.4, 3.6, 5, and 10 μm; depth h: 100 nm).

Experimental realization

In the experiment, a tunable continuous wave laser source is used to scan the fabricated device working at different wavelengths. Figure 4I shows the experimental setup for characterizing the fabricated chip-scale broadband polarization diversity OAM generator on a silicon platform. The laser output is divided into two branches via a 3-dB coupler. One branch with its polarization controlled by a polarization controller (PC) is used to excite the in-plane TE_0 mode guided in the fabricated chip-scale silicon OAM generator (OAM chip) via a lensed fiber (end coupling). The in-plane guided TE_0 mode in the silicon waveguide is coupled out by the subwavelength surface structure (superposed holographic fork gratings) into free space and converted to polarization diversity OAM mode (x-pol. OAM_{+1}, x-pol. OAM_{-1}, y-pol. OAM_{+1}, y-pol. OAM_{-1}), which is collimated by an objective lens. Another lens is adopted to adjust the beam size. The other branch serves as a reference Gaussian beam. The power and polarization of the reference Gaussian beam are adjusted by use of a PC, a variable optical attenuator (VOA), a collimator, a polarizer, and a half-wave plate (HWP). The generated polarization diversity OAM mode and the reference Gaussian beam with the same polarization, proper relative power and beam size are combined through a beam splitter to produce the interferogram. The wavelength tuning range of the laser is from 1500 to 1630 nm. The attenuation tuning range of the VOA is from 2 to 60 dB. We use a camera to monitor the intensity profiles of generated OAM modes and their corresponding interferograms.

We demonstrate the generation of broadband polarization diversity OAM modes using the fabricated device. Figure 4J shows measured results (intensity profile and interferogram) for the generation of x-pol. OAM_{+1}, x-pol. OAM_{-1}, y-pol. OAM_{+1}, and y-pol. OAM_{-1} in the C-band (1530 to 1565 nm). One can confirm the order (magnitude and sign) of the generated OAM modes from the number of twists and twist direction of the interferograms. To verify the generation of x-pol. and y-pol. OAM modes, we insert a polarizer before the camera (not shown in Fig. 4J). Figure 4K shows measured intensity profiles when rotating the polarizer direction to 90° (vertical), 45° and 0° (horizontal). The generated x-pol. OAM_{+1} is confirmed from the observed gradually increased power from the minimum to the maximum. Similarly, one can also verify the generation of y-pol. OAM_{+1} with its power variation after rotating the polarizer from the maximum to the minimum. Beyond C-band (1530 to 1565 nm), we also demonstrate the ultrabroadband generation of OAM mode from 1500 to 1630 nm with a wide wavelength range of 130 nm (limited by the available laser source used in the experiment), as shown in Fig. 4K.

We characterize the mode quality and efficiency in the experiment. For the generated OAM mode having distinct spiral phase structure, here, we focus more on the evaluation of the phase purity. We need to obtain the phase profile of the generated OAM mode to measure the phase purity. Note that the phase profile could not be directly observed. Instead, we can use the Fourier transform method (*40*) (see Materials and Methods) to reconstruct the phase profile of the generated OAM mode by measuring a tilt interferogram with fork interference fringe. Taking the broadband (1500 to 1630 nm) generation of y-pol. OAM_{+1} as one example, as shown in Fig. 5A, the first column shows the measured intensity profiles at 1500, 1550, 1600, and 1630 nm, from which one can see the donut shape with null intensity at the beam center due to the phase singularity. The second column shows the measured collinear interferograms (collinear interference between the OAM mode and a reference Gaussian beam), from which one can confirm the successful generation of y-pol. OAM_{+1} with good performance (clear number of twists and twist direction) over a wide wavelength range from 1500 to 1630 nm. The third column shows the measured tilt interferograms (tilt interference between the OAM mode and a reference Gaussian beam), which have fork structures at the beam center. The fourth column shows phase reconstruction from the measured tilt interferograms using the Fourier transform method. After spherical correction (see Materials and Methods), one can see the spiral phase structure with azimuthal phase change from 0 to 2π, indicating the generation of OAM_{+1} mode. Figure 5B depicts the measured phase purity of the generated y-pol. OAM_{+1} as a function of the wavelength from 1500 to 1630 nm. The measured maximum and minimum phase purities are about 0.90 at 1620 nm and 0.85 at 1500 nm, respectively. The broadband generation of OAM mode with high purity over a wide wavelength range

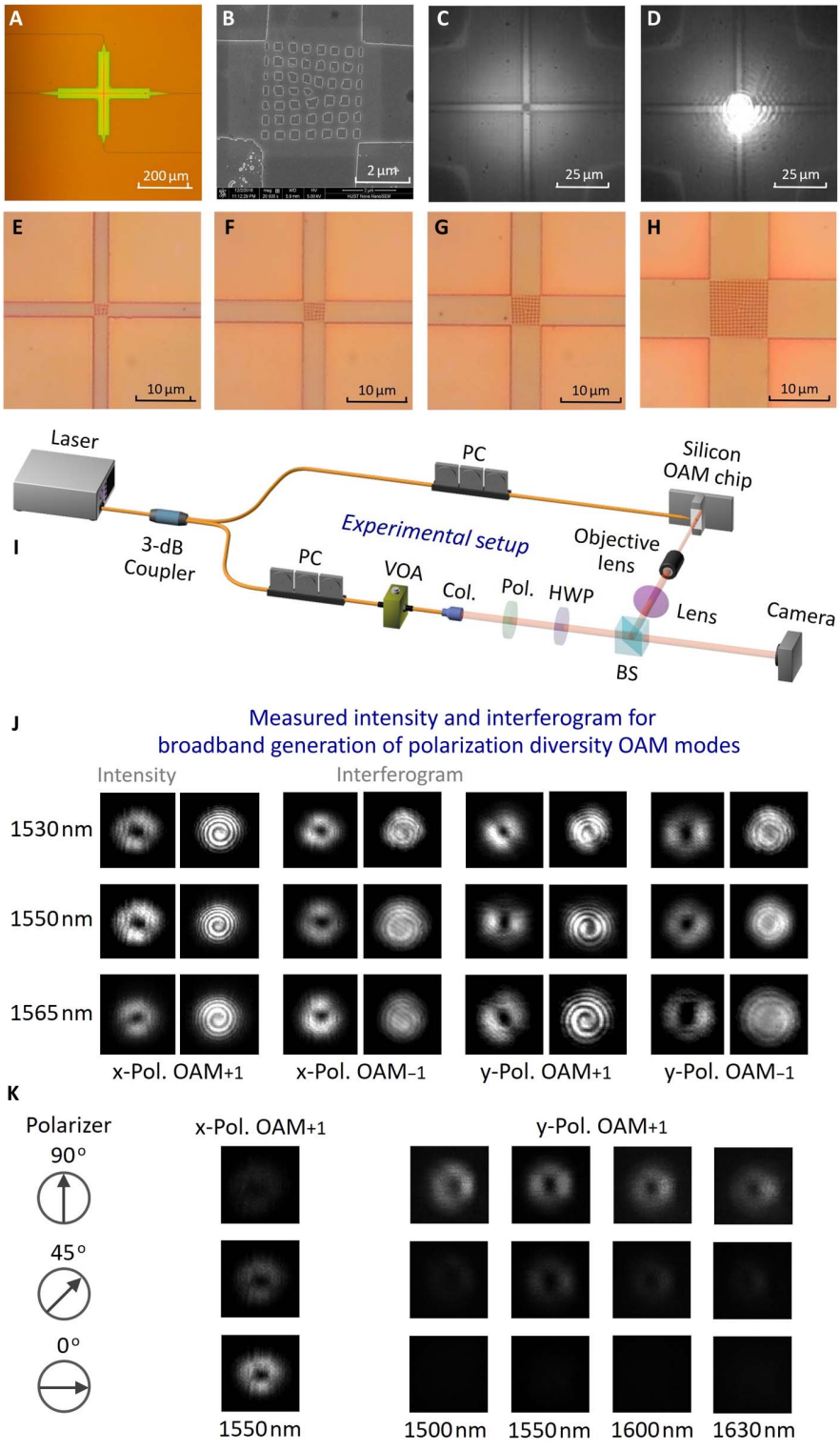

Fig. 4. Fabricated devices, experimental setup, and measured results for the generation of broadband polarization diversity OAM modes. (**A**) Measured optical microscope image of the layout of superposed holographic fork gratings connected by four adiabatic tapers. (**B**) Measured SEM image of the superposed holographic fork grating region. (**C**) Measured optical microscope image of the device without incidence of the in-plane guided mode. (**D**) Measured near-field view (bright spot from the center grating region) for generating y-pol. OAM_{-1} with incidence of the in-plane guided mode. (**E** to **H**) Measured optical microscope images of the fabricated devices with different lengths of the grating region of 2.4 μm (E), 3.6 μm (F), 5 μm (G), and 10 μm (H). (**I**) Experimental setup. PC, polarization controller; VOA, variable optical attenuator; Col., collimator; Pol., polarizer; HWP, half-wave plate; BS, beam splitter. (**J**) Measured far-field intensity profiles and interferograms for the broadband generation of polarization diversity OAM modes (x-pol. OAM_{+1}, x-pol. OAM_{-1}, y-pol. OAM_{+1}, y-pol. OAM_{-1}) in the C-band. (**K**) Measured far-field intensity profiles of x-pol. OAM_{+1} (1550 nm) and y-pol. OAM_{+1} (1500, 1550, 1600, 1630 nm) after a rotating polarizer (90°, 45°, 0°).

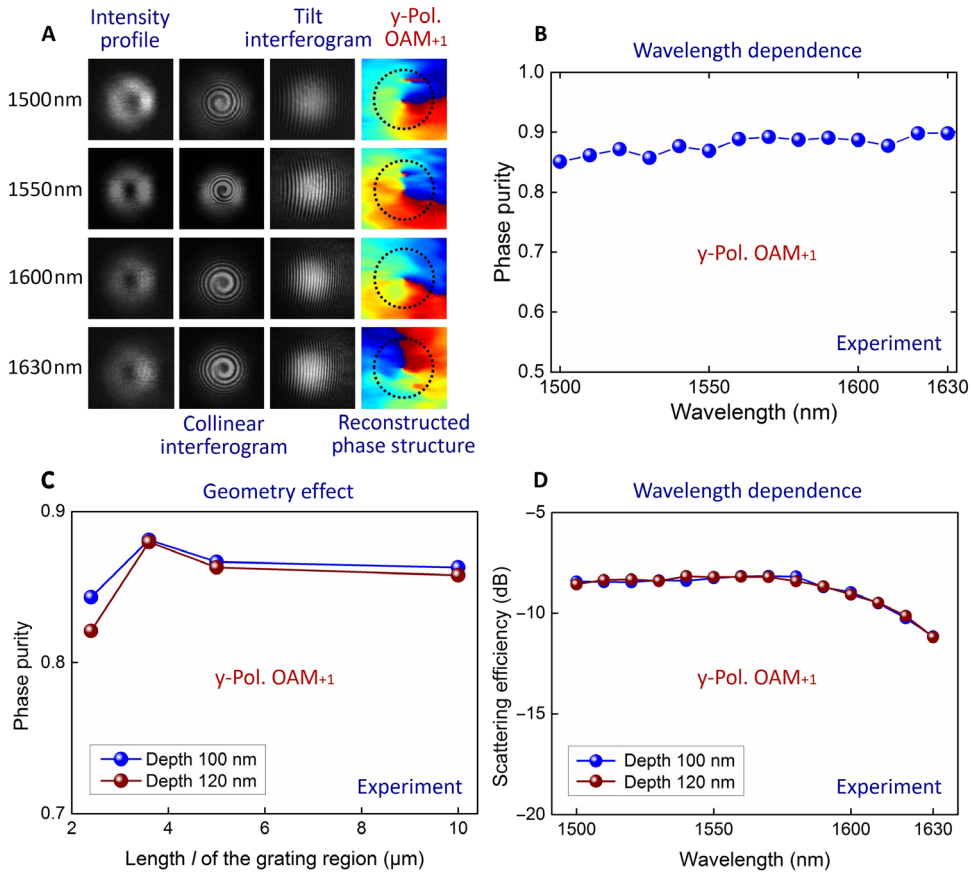

Fig. 5. Experimental measurements of the phase reconstruction, phase purity, and scattering efficiency for the generation of polarization diversity OAM modes. (**A**) Measured far-field intensity profiles, collinear interferograms, tilt interferograms, and reconstructed phase structures of the generated y-pol. OAM_{+1} at 1500, 1550, 1600, and 1630 nm. (**B**) Measured phase purity of the generated y-pol. OAM_{+1} versus wavelength (1500 to 1630 nm). (**C**) Measured phase purity of the generated y-pol. OAM_{+1} versus length *l* of the grating region with two depths of 100 and 120 nm. (**D**) Measured scattering efficiency of the generated y-pol. OAM_{+1} versus wavelength with two depths of 100 and 120 nm.

from 1500 to 1630 nm in the experiment is in good agreement with the theory, as shown in Fig. 2D. The device used in Fig. 5 (A and B) has a length of the grating region of 3.6 μm and a depth of 60 nm. In the experiment, we also measure the phase purity of the generated OAM mode (y-pol. OAM_{+1} as one example) from the fabricated devices with different lengths of the grating region of 2.4, 3.6, 5, and 10 μm and different etching depths of 100 and 200 nm. As shown in Fig. 5C, one can see the slight variation of the measured phase purity when the length of the grating region is changed from 2.4 to 10 μm. An optimized phase purity is observed with a length of the grating region of 3.6 μm. Figure 5D shows the measured scattering efficiency (y-pol. OAM_{+1}) using devices with different depths of 100 and 120 nm. For the device with a depth of 100 nm, the measured efficiency is −8.27 dB at 1550 nm. For the device with a depth of 120 nm, the measured efficiency is −8.21 dB at 1550 nm. The experimental results shown in Fig. 5 (C and D) agree well with the simulation results shown in Fig. 2 (B and H). We obtain similar trends in the experiments for the length-dependent purity and wavelength-dependent efficiency compared to the simulations. We also demonstrate broadband generation of OAM mode. The relatively lower efficiency measured in the experiments compared to that in the simulations might be due to the waveguide propagation loss and defects of the device induced in the fabrication process. Future optimization of the fabrication technique may further improve the efficiency of the polarization diversity OAM generator.

The phase purity only shows the quality of the generated OAM mode itself. To show their influence on each other, we further characterize the cross-talk matrix and accumulated cross-talk (see Materials and Methods) for the generation of polarization diversity OAM modes (x-pol. OAM_{+1}, x-pol. OAM_{-1}, y-pol. OAM_{+1}, y-pol. OAM_{-1}). We update the experimental configuration when measuring the cross-talk matrix and accumulated cross-talk. As shown in Fig. 6A, the generated polarization diversity OAM mode is vertically emitted to free space and collimated by an objective lens. After that, we use the combination of a polarizer and an SLM to demodulate the polarization diversity OAM modes (x-pol. OAM_{+1}, x-pol. OAM_{-1}, y-pol. OAM_{+1}, y-pol. OAM_{-1}). We place an HWP between the polarizer and SLM to adjust the polarization state after the polarizer to be aligned to the working direction of the polarization-sensitive SLM. We use a lens between the HWP and SLM to appropriately adjust the beam size projected onto the SLM. The polarizer detects the polarization state of the generated OAM mode. Two kinds of phase patterns are loaded onto the SLM to detect either OAM_{+1} or OAM_{-1} mode. After the SLM, we use a flip mirror to switch the optical path either to a camera or to an optical power meter. We use a collimator to couple the demodulated Gaussian-like beam into a piece of fiber connected to the power meter. The camera monitors the

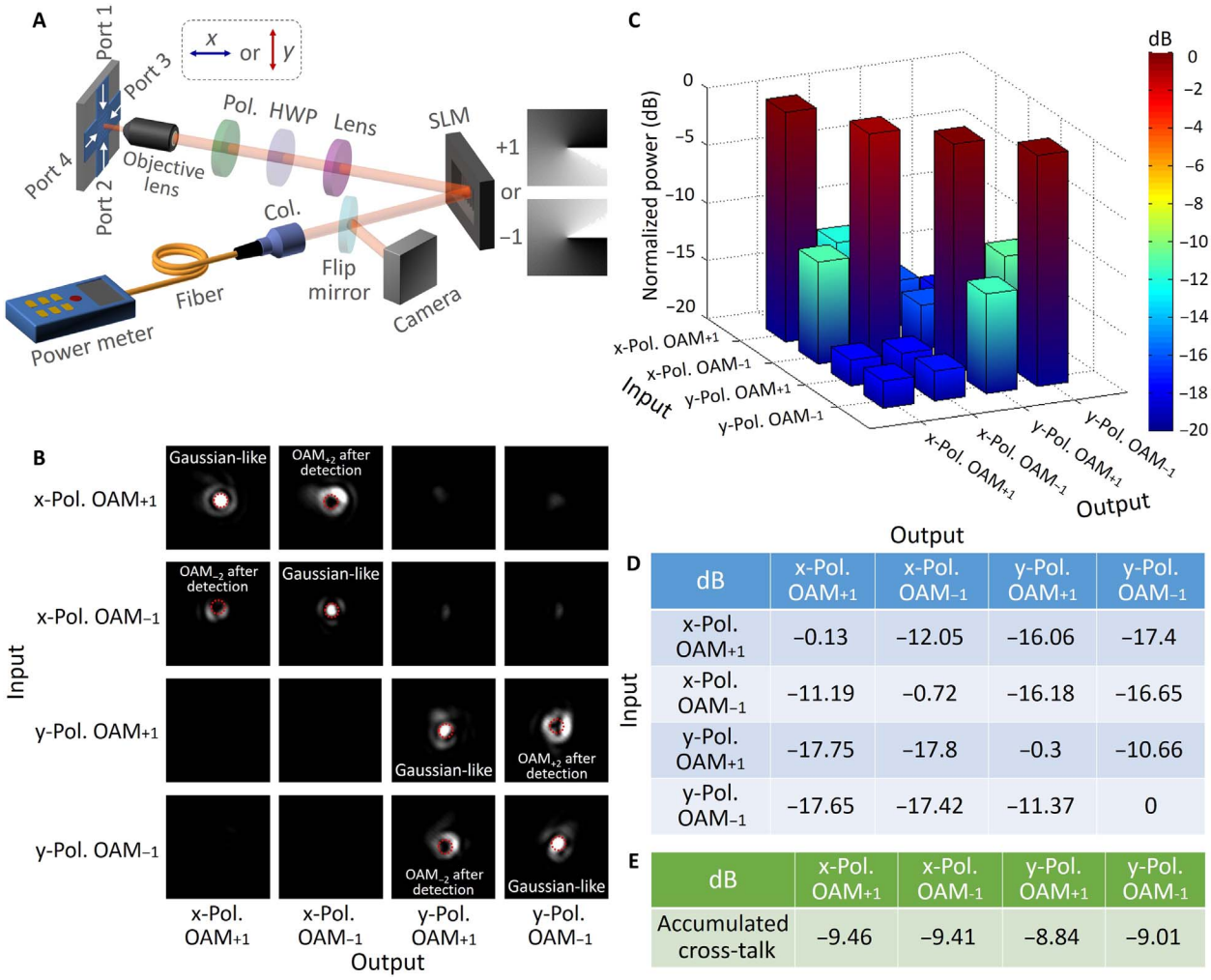

D dB	x-Pol. OAM+1	x-Pol. OAM−1	y-Pol. OAM+1	y-Pol. OAM−1
x-Pol. OAM+1	−0.13	−12.05	−16.06	−17.4
x-Pol. OAM−1	−11.19	−0.72	−16.18	−16.65
y-Pol. OAM+1	−17.75	−17.8	−0.3	−10.66
y-Pol. OAM−1	−17.65	−17.42	−11.37	0

E dB	x-Pol. OAM+1	x-Pol. OAM−1	y-Pol. OAM+1	y-Pol. OAM−1
Accumulated cross-talk	−9.46	−9.41	−8.84	−9.01

Fig. 6. Experimental measurements of the cross-talk matrix and accumulated cross-talk for the generation of polarization diversity OAM modes (x-pol. OAM_{+1}, x-pol. OAM_{-1}, y-pol. OAM_{+1}, y-pol. OAM_{-1}). (**A**) Experimental configuration. Pol., polarization; HWP, half-wave plate; SLM, spatial light modulator; Col., Collimator. (**B**) Measured 4 × 4 intensity distribution matrix. (**C**) Measured histograms of the 4 × 4 cross-talk matrix. (**D**) Measured 4 × 4 cross-talk matrix. (**E**) Measured accumulated cross-talk summing up all the noise (all the unwanted channels are on at the same time).

intensity distribution for the demodulation of polarization diversity OAM modes, while the power meter records the demodulated power values to measure the cross-talk matrix. As shown in Fig. 6A, we have four input ports, each corresponding to the generation of one desired OAM mode. For the detection, the polarizer is set at two directions (x- or y-polarization) to detect x-pol. or y-pol., while the SLM is loaded with two phase patterns to detect OAM_{+1} or OAM_{-1}. Hence, the combined polarizer and SLM give four outputs by adjusting polarizer and SLM. With incident light to each input port, four output intensity distribution images are monitored by the camera, and four output powers are recorded by the power meter; therefore, we obtain a 4 × 4 intensity distribution matrix and a 4 × 4 cross-talk matrix. Figure 6B shows the measured 4 × 4 intensity distribution matrix. The simulated 4 × 4 intensity distribution matrix is shown in fig. S3. The experimental results are in good agreement with theoretical ones. The diagonal elements (1,1), (2,2), (3,3), and (4,4) in the matrix correspond to the correct detection of both polarization state and OAM state. Note that the correct detection of the OAM state by loading an inverse phase pattern onto the SLM converts the spiral phase front back to a planar phase front and gives a bright spot at the beam center (Gaussian-like beams with central spot shown in the diagonal of the 4 × 4 matrix). In contrast, when the OAM mode is not detected using the right phase pattern (nondiagonal elements in the 4 × 4 matrix), after the SLM, it is still an OAM mode but with an updated charge value and a donut-shaped intensity distribution. For example, the nondiagonal elements (2,1) and (1,2) are actually intensity profiles of updated OAM modes of OAM_{-2} (OAM_{-1} detected by charge −1 phase pattern) and OAM_{+2} (OAM_{+1} detected by charge +1 phase pattern). The updated OAM modes show donut-shaped intensity distribution with null intensity at the beam center. The diagonal elements have central spots, while the nondiagonal elements have null intensity at the center. When using a piece of fiber (Fig. 6A) for spatial filtering (red dashed circles in Fig. 6B), the diagonal elements with central spots can be coupled into the fiber for power measurement, while the nondiagonal elements with null intensity at the center will be blocked by the fiber (*12*). Figure 6 (C and D) shows the recorded 4 × 4 cross-talk matrix, which can evaluate the influence on each other for the generation of polarization diversity OAM modes. By summing up all the noise, i.e., all the unwanted channels are on at the same time, the

real accumulated cross-talk can be eventually obtained from the measured 4 × 4 cross-talk matrix. As shown in Fig. 6E, for the generation of polarization diversity OAM modes, the real accumulated cross-talk is measured to be approximately −9.46 dB for x-pol. OAM_{+1}, −9.41 dB for x-pol. OAM_{-1}, −8.84 dB for y-pol. OAM_{+1}, and −9.01 dB for y-pol. OAM_{-1}. One can see from Fig. 6 that favorable performance is achieved in the experiment for the generation of polarization diversity OAM modes. The obtained theoretical and experimental results shown in Figs. 2 to 6 indicate the successful implementation of an ultra-compact (3.6 × 3.6 μm^2 footprint) broadband polarization diversity OAM generator with favorable operation performance.

DISCUSSION

In summary, we propose, design, fabricate, and demonstrate an ultra-compact broadband polarization diversity OAM generator formed by introducing a subwavelength surface structure (superposed holographic fork gratings) on top of a silicon waveguide. The working principle relies on the mode coupling from the in-plane waveguide mode to the out-plane free-space OAM mode by the subwavelength surface structure. This configuration of in-plane input and out-plane output with vertical emission facilitates possible 2D array integration. The broadband property benefits from the subwavelength surface structure. The superposition of two orthogonal holographic fork gratings benefits the polarization diversity property. We demonstrate both in theory and experiment the chip-scale broadband polarization diversity OAM generation on a silicon platform with an ultra-compact 3.6 × 3.6 μm^2 footprint. The generated polarization diversity x-pol. OAM_{+1}, x-pol. OAM_{-1}, y-pol. OAM_{+1}, and y-pol. OAM_{-1} show favorable operation performance with relatively high purity and efficiency within a wide wavelength range from 1500 to 1630 nm. These demonstrations on a broadband polarization diversity OAM generator provide the possibility of simultaneously accessing and fully exploiting multiple physical dimensions of light such as wavelength, polarization, and spatial structure. Several future perspectives toward more robust devices and grooming applications could be considered as follows.

1) Devices with higher purity and higher efficiency

Although relatively high purity and high efficiency are achieved in the present design, one may expect higher purity and higher efficiency by future optimization. Taking the scattering efficiency as an example, the downward emission to the substrate, the transmitted light and reflected light by the grating are the main factors limiting the efficiency of the OAM generator. For the downward emission to the substrate, adding a reflection layer could be an efficient solution, which has been verified by simulations in Fig. 2 (E and F). Future fabrication of this OAM generator adding a reflector is expected. For the transmitted light and reflected light by the grating, one may learn from the traditional blazed holographic grating and appropriately design a complex phase grating (not binary phase but varied phase) on top of the silicon waveguide to greatly reduce the unwanted terms of the output field. Moreover, inverse design with the target higher purity and higher efficiency might be considered. In addition, further optimization of the fabrication technique may also benefit higher purity and higher efficiency of the OAM generator as designed.

2) Devices supporting high-order OAM modes and multiple OAM modes

Based on the same principle of holographic method, one could also design the polarization diversity high-order OAM mode generator. Moreover, 3D photonic integrated structures with multiple layers could be adopted to generate multiple OAM modes with polarization diversity OAM ± ℓ (the same | ℓ |) emitted by each layer.

3) Devices with more input ports

Most of the previous works on chip-scale OAM generators have two ports and only single-polarization OAM is generated. Here, we introduce the superposition of two orthogonal holographic fork gratings on a silicon platform with four input ports. As a result, a polarization diversity OAM generator is implemented. Devices with more than four input ports might offer advanced functions (e.g., generation of multiple OAM modes). Complex gratings and inverse design could be considered.

4) Devices supporting fiber packaging

To facilitate the potential fiber-based OAM applications, the packaging of the silicon OAM chip and fibers is of great interest. The input ports of the silicon OAM chip could be connected to single-mode fibers. The emitted OAM modes could be coupled to a specific fiber supporting them. The mode matching is important. High-efficient and compact device-fiber packaging with input and output fibers is full of challenges but is worth studying.

5) Applications in N-dimensional optical communications or interconnects with OAM multiplexing

The presented broadband polarization diversity OAM generator has distinct advantages of being fully compatible with the existing multiplexing techniques such as wavelength-division multiplexing and polarization-division multiplexing. The demonstrated broadband operation (1500 to 1630 nm limited by the available laser source) and polarization diversity operation (x-pol. OAM_{+1}, x-pol. OAM_{-1}, y-pol. OAM_{+1}, y-pol. OAM_{-1}) with favorable performance indicate that one may use the designed silicon OAM chip to fully exploit hundreds of wavelengths covering the whole C + L communication band (1530 to 1625 nm), two polarizations, and two OAM modes for multiplexing. Similarly, one may also use the device in an opposite way for demultiplexing, that is, when using the designed silicon OAM chips as (de) multiplexers, N-dimensional (wavelength, polarization, and OAM) optical multiplexing communications or interconnects are possible with a tremendous increase of aggregate transmission capacity.

6) Applications in synthesis of OAM modes

The designed polarization diversity OAM generator may also function as a robust OAM synthesizer with coherent launching from multiple input ports. The chip-scale OAM synthesizer may enable the generation of other spatial modes such as linearly polarized mode (e.g., Fig. 1G+Fig. 1H or Fig. 1I+Fig. 1J), which is widely used in fiber-based SDM communications. The chip-scale OAM synthesizer may also enable the generation of OAM beams with arbitrary polarization states (e.g., Fig. 1G+Fig. 1I or Fig. 1H+Fig. 1J, with relative power and phase control). For example, the combination of x-pol. OAM_{+1} (Fig. 1G) and y-pol. OAM_{+1} (Fig. 1I) with a relative $\pi/2$ phase shift can produce a circularly polarized OAM mode, carrying both SAM and OAM. Moreover, the chip-scale OAM synthesizer can also potentially be used in quantum applications such as quantum key distribution (QKD). Compared with most of the current QKD schemes only relying on polarization encoding, OAM-based QKD systems show the promise of providing an enhanced tolerance to errors and, therefore, the potential for a quantum communication channel that is more robust against eavesdropping. The chip-scale OAM synthesizer may offer an ultra-compact solution to the generation of OAM superposition states accessing both polarization and OAM physical dimensions, which is of great interest for high-dimensional OAM-assisted quantum communication systems.

MATERIALS AND METHODS

Mode purity

To evaluate the quality of the generated OAM mode itself, the mode purity is introduced as follows

$$p = \frac{\left| \int A_0^*(x,y,z) A_t(x,y,z) dxdydz \right|^2}{\int |A_0(x,y,z)|^2 dxdydz \int |A_t(x,y,z)|^2 dxdydz} \quad (10)$$

where $A_0(x, y, z)$ and $A_t(x, y, z)$ are the complex amplitudes of the obtained mode and target mode, respectively. The phase purity focuses more on the spatial phase structure.

Scattering efficiency

For the generation of polarization diversity OAM modes based on the subwavelength surface structure (superposed holographic fork gratings) on top of a silicon waveguide, the scattering efficiency is defined as the power ratio of the emitted OAM mode from the device to the incident coupled in-plane guided mode.

Cross-talk matrix and accumulated cross-talk

To assess the influence on each other for the generation of polarization diversity OAM modes, the cross-talk matrix and accumulated cross-talk can be measured. In general, the accumulated cross-talk is defined as the ratio of the coupled power from all unwanted channels (all unwanted channels on, desired channel off) to the power of the desired channel (all unwanted channels off, desired channel on). For the polarization diversity OAM generator (x-pol. OAM_{+1}, x-pol. OAM_{-1}, y-pol. OAM_{+1}, y-pol. OAM_{-1}) with four input ports, each corresponding to the generation of one OAM mode, the combined use of a polarizer (detecting x-pol. or y-pol.) and an SLM (detecting OAM_{+1} or OAM_{-1}) at the receiver gives four outputs, each corresponding to the correct detection of one specific OAM mode. For each input, we record four outputs, and therefore, a 4 × 4 cross-talk matrix is obtained. The diagonal elements in the matrix correspond to the correct detection of both polarization state and OAM state, while other nondiagonal elements in the matrix reflect the cross-talk among four polarization diversity OAM modes. The accumulated cross-talk summing up all the noise (all the unwanted channels are on) can be obtained by measuring the cross-talk matrix. The cross-talk matrix measurement provides an easy way to evaluate the influence among different polarization diversity OAM modes.

Phase reconstruction by Fourier transform method

On the basis of the theory of interference, the intensity of the tilt interference between an OAM mode and a reference Gaussian light can be expressed as

$$I_I = a + b\cos(\ell\theta + 2\pi f_0 x) \quad (11)$$

where $a = I_O + I_G$ and $b = 2\sqrt{I_O \cdot I_G}$; I_I, I_O, and I_G are the intensity of the interference field, OAM mode, and reference Gaussian light, respectively; and $f_0 = \sin\phi/\lambda$ is the spatial frequency caused by tilt interference with an angle of ϕ and a wavelength of λ. Equation 11 can be written in a complex field as follows based on the Euler formula

$$I_I = a + c \cdot \exp(i2\pi f_0 x) + c^* \cdot \exp(-i2\pi f_0 x) \quad (12)$$

where $c = b \cdot \exp(i\ell\theta)/2$. After taking the Fourier transform for both sides, Eq. 12 can be written as

$$\mathcal{F}(I_I) = A(f) + C \cdot (f - f_0) + C^* \cdot (f + f_0) \quad (13)$$

where $\mathcal{F}$, A, and C are the Fourier transforms of I_I, a, and c, respectively. By picking up C at the frequency of $f = f_0$ with a high-pass filter and performing Fourier inverse transform, one can obtain $c = b \cdot \exp(i\ell\theta)/2$. Last, by extracting the imaginary part of C, the phase profile of the OAM mode can be reconstructed.

Spherical correction

In practical measurements, the reconstructed phase profile always consists of two parts. One is the intrinsic spiral phase distribution of an OAM mode, and the other is the spherical phase distribution induced by propagation. To measure the phase purity, we needed to subtract the corresponding spherical phase distribution to obtain the desired spiral phase distribution. When exciting both OAM_{+1} and OAM_{-1} with the same polarization, the superposed OAM_{+1} and OAM_{-1} cancel the spiral phase distribution but preserve the spherical phase distribution, which is similar to that of a single OAM mode. Using the same Fourier transform method for the tilt interference between the superposed OAM_{+1} and OAM_{-1} and a reference Gaussian light, one can retrieve the spherical phase distribution induced by propagation. By subtracting the spherical phase distribution from the extracted phase profile of the OAM mode, one can realize the spherical correction and lastly retrieve the intrinsic spiral phase distribution of the generated OAM mode. To measure the phase purity, one can calculate the overlap integral between the extracted spiral phase distribution and an ideal one.

SUPPLEMENTARY MATERIALS

Supplementary material for this article is available at http://advances.sciencemag.org/cgi/content/full/5/5/eaau9593/DC1

Section S1. Evolution process of in-plane guided mode to out-plane OAM mode

Section S2. Device fabrication process

Section S3. Simulated intensity distribution matrix

Fig. S1. Simulated 3D-FDTD results of electric field distributions (real part of electric field components) along the waveguide (from waveguide region to grating region) and at different height of the fork grating region (z = 0.1, 0.2, 0.3, 0.4, 0.5 μm, far field).

Fig. S2. Illustration of the device fabrication process of the silicon OAM generator (spin coating, electron-beam lithography, inductively coupled plasma, photoresist removal).

Fig. S3. Simulated 4 × 4 intensity distribution matrix for the generation of polarization diversity OAM modes (x-pol. OAM_{+1}, x-pol. OAM_{-1}, y-pol. OAM_{+1}, y-pol. OAM_{-1}).

REFERENCES AND NOTES

1. L. Allen, M. W. Beijersbergen, R. J. C. Spreeuw, J. P. Woerdman, Orbital angular momentum of light and the transformation of Laguerre–Gaussian laser modes. *Phys. Rev. A* **45**, 8185–8189 (1992).
2. A. M. Yao, M. J. Padgett, Orbital angular momentum: Origins, behavior and applications. *Adv. Opt. Photonics* **3**, 161–204 (2011).
3. M. Padgett, R. Bowman, Tweezers with a twist. *Nat. Photonics* **5**, 343–348 (2011).
4. S. Fürhapter, A. Jesacher, S. Bernet, M. Ritsch-Marte, Spiral phase contrast imaging in microscopy. *Opt. Express* **13**, 689–694 (2005).
5. L. Fang, M. J. Padgett, J. Wang, Sharing a common origin between the rotational and linear Doppler effects. *Laser Photonics Rev.* **11**, 1700183 (2017).
6. N. M. Elias II, Photon orbital angular momentum in astronomy. *Astron. Astrophys.* **492**, 883–922 (2008).
7. J. Vieira, R. M. G. M. Trines, E. P. Alves, R. A. Fonseca, J. T. Mendonça, R. Bingham, P. Norreys, L. O. Silva, Amplification and generation of ultra-intense twisted laser pulses via stimulated Raman scattering. *Nat. Commun.* **7**, 10371 (2016).

8. J. Leach, B. Jack, J. Romero, A. K. Jha, A. M. Yao, S. Franke-Arnold, D. G. Ireland, R. W. Boyd, S. M. Barnett, M. J. Padgett, Quantum correlations in optical angle-orbital angular momentum variables. *Science* **329**, 662–665 (2010).
9. J. Wang, Advances in communications using optical vortices. *Photonics Res.* **4**, B14–B28 (2016).
10. J. Wang, Data information transfer using complex optical fields: A review and perspective (Invited Paper). *Chin. Opt. Lett.* **15**, 030005 (2017).
11. J. Wang, Twisted optical communications using orbital angular momentum. *Sci. Chin. Phys. Mech. Astron.* **62**, 034201 (2019).
12. J. Wang, J.-Y. Yang, I. M. Fazal, N. Ahmed, Y. Yan, H. Huang, Y. Ren, Y. Yue, S. Dolinar, M. Tur, A. E. Willner, Terabit free-space data transmission employing orbital angular momentum multiplexing. *Nat. Photonics* **6**, 488–496 (2012).
13. N. Bozinovic, Y. Yue, Y. Ren, M. Tur, P. Kristensen, H. Huang, A. E. Willner, S. Ramachandran, Terabit-scale orbital angular momentum mode division multiplexing in fibers. *Science* **340**, 1545–1548 (2013).
14. A. Wang, L. Zhu, L. Wang, J. Ai, S. Chen, J. Wang, Directly using 8.8-km conventional multi-mode fiber for 6-mode orbital angular momentum multiplexing transmission. *Opt. Express* **26**, 10038–10047 (2018).
15. Y. Ren, L. Li, Z. Wang, S. M. Kamali, E. Arbabi, A. Arbabi, Z. Zhao, G. Xie, Y. Cao, N. Ahmed, Y. Yan, C. Liu, A. J. Willner, S. Ashraf, M. Tur, A. Faraon, A. E. Willner, Orbital angular momentum-based space division multiplexing for high-capacity underwater optical communications. *Sci. Rep.* **6**, 33306 (2016).
16. A. Wang, L. Zhu, Y. Zhao, S. Li, W. Lv, J. Xu, J. Wang, Adaptive water-air-water data information transfer using orbital angular momentum. *Opt. Express* **26**, 8669–8678 (2018).
17. Y. Zhao, C. Cai, J. Zhang, X. Cao, L. Wang, S. Li, J. Wang, Feedback-enabled adaptive underwater twisted light transmission link utilizing the reflection at the air-water interface. *Opt. Express* **26**, 16102–16112 (2018).
18. D. J. Richardson, J. M. Fini, L. E. Nelson, Space-division multiplexing in optical fibres. *Nat. Photonics* **7**, 354–362 (2013).
19. M. Okida, T. Omatsu, M. Itoh, T. Yatagai, Direct generation of high power Laguerre-Gaussian output from a diode-pumped Nd:YVO_4 1.3-μm bounce laser. *Opt. Express* **15**, 7616–7622 (2007).
20. M. W. Beijersbergen, L. Allen, H. E. L. O. van der Veen, J. P. Woerdman, Astigmatic laser mode converters and transfer of orbital angular momentum. *Opt. Commun.* **96**, 123–132 (1993).
21. L. Marrucci, E. Karimi, S. Slussarenko, B. Piccirillo, E. Santamato, E. Nagali, F. Sciarrino, Spin-to-orbital conversion of the angular momentum of light and its classical and quantum applications. *J. Opt* **13**, 064001 (2011).
22. S. S. R. Oemrawsingh, J. A. W. van Houwelingen, E. R. Eliel, J. P. Woerdman, E. J. K. Verstegen, J. G. Kloosterboer, G. W. 't Hooft, Production and characterization of spiral phase plates for optical wavelengths. *Appl. Optics* **43**, 688–694 (2004).
23. A. Forbes, A. Dudley, M. McLaren, Creation and detection of optical modes with spatial light modulators. *Adv. Opt. Photonics* **8**, 200–227 (2016).
24. S. Li, Q. Mo, X. Hu, C. Du, J. Wang, Controllable all-fiber orbital angular momentum mode converter. *Opt. Lett.* **40**, 4376–4379 (2015).
25. T. Su, R. P. Scott, S. S. Djordjevic, N. K. Fontaine, D. J. Geisler, X. Cai, S. J. B. Yoo, Demonstration of free space coherent optical communication using integrated silicon photonic orbital angular momentum devices. *Opt. Express* **20**, 9396–9402 (2012).
26. X. Cai, J. Wang, M. J. Strain, B. Johnson-Morris, J. Zhu, M. Sorel, J. L. O'Brien, M. G. Thompson, S. Yu, Integrated compact optical vortex beam emitters. *Science* **338**, 363–366 (2012).
27. P. Miao, Z. Zhang, J. Sun, W. Walasik, S. Longhi, N. M. Litchinitser, L. Feng, Orbital angular momentum microlaser. *Science* **353**, 464–467 (2016).
28. A. Liu, C.-L. Zou, X. Ren, Q. Wang, G.-C. Guo, On-chip generation and control of the vortex beam. *Appl. Phys. Lett.* **108**, 181103 (2016).
29. J. Du, J. Wang, Chip-scale optical vortex lattice generator on a silicon platform. *Opt. Lett.* **42**, 5054–5057 (2017).
30. C. T. Nadovich, W. D. Jemison, D. J. Kosciolek, D. T. Crouse, Focused apodized forked grating coupler. *Opt. Express* **25**, 26861–26874 (2017).
31. Z. Xie, T. Lei, F. Li, H. Qiu, Z. Zhang, H. Wang, C. Min, L. Du, Z. Li, X. Yuan, Ultra-broadband on-chip twisted light emitter for optical communications. *Light Sci. Appl.* **7**, 18001 (2018).
32. N. Zhou, S. Zheng, X. Cao, S. Gao, S. Li, M. He, X. Cai, J. Wang, Generating and synthesizing ultrabroadband twisted light using a compact silicon chip. *Opt. Lett.* **43**, 3140–3143 (2018).
33. N. Yu, P. Genevet, M. A. Kats, F. Aieta, J.-P. Tetienne, F. Capasso, Z. Gaburro, Light propagation with phase discontinuities: Generalized laws of reflection and refraction. *Science* **334**, 333–337 (2011).
34. Y. Zhao, J. Du, J. Zhang, L. Shen, J. Wang, Generating structured light with phase helix and intensity helix using reflection-enhanced plasmonic metasurface at 2 μm. *Appl. Phys. Lett.* **112**, 171103 (2018).
35. J. Wang, Metasurfaces enabling structured light manipulation: Advances and perspectives [Invited]. *Chin. Opt. Lett.* **16**, 050006 (2018).
36. J. Wang, Y. Long, On-chip silicon photonic signaling and processing: A review. *Sci. Bull.* **63**, 1267–1310 (2018).
37. N. R. Heckenberg, R. McDuff, C. P. Smith, H. Rubinsztein-Dunlop, M. J. Wegener, Laser beams with phase singularities. *Opt. Quantum Electron.* **24**, S951–S962 (1992).
38. L. Janicijevic, S. Topuzoski, Fresnel and Fraunhofer diffraction of a Gaussian laser beam by fork-shaped gratings. *J. Opt. Soc. Am. A* **25**, 2659–2669 (2008).
39. Y. Ding, C. Peucheret, H. Ou, K. Yvind, Fully etched apodized grating coupler on the SOI platform with −0.58 dB coupling efficiency. *Opt. Lett.* **39**, 5348–5350 (2014).
40. C. Roddier, F. Roddier, Interferogram analysis using Fourier transform techniques. *Appl. Opt.* **26**, 1668–1673 (1987).

Acknowledgments: We thank J. Liu for technical support and helpful discussions. **Funding:** This work was supported by the National Natural Science Foundation of China (NSFC) (11574001, 61761130082, 11774116, 11274131, 61222502, 11690031, and 61575224), the National Basic Research Program of China (973 Program) (2014CB340004), the Royal Society-Newton Advanced Fellowship, the National Program for Support of Top-notch Young Professionals, the Yangtze River Excellent Young Scholars Program, the Natural Science Foundation of Hubei Province of China (2018CFA048), the Key R&D Program of Guangdong Province (2018B030325002), the Local Innovative and Research Teams Project of Guangdong Pearl River Talents Program (2017BT01X121), and the Program for HUST Academic Frontier Youth Team (2016QYTD05). **Author contributions:** J.W. developed the concept. J.W. and N.Z. designed the photonic integrated devices and conceived the experiments. N.Z., S.Z., and X. Cao carried out the experiments. J.W. and N.Z. performed the theoretical analyses, simulations, acquired the experimental data, and carried out the data analyses. S.G., Y. Zhu, M.H., and X. Cai fabricated the devices. X. Cai and Y. Zhao provided the technical support in the experiments. J.W. and N.Z. contributed to writing the paper. J.W. finalized the paper. J.W. supervised the project. **Competing interests:** The authors declare that they have no competing interests. **Data and materials availability:** All data needed to evaluate the conclusions in the paper are present in the paper and/or the Supplementary Materials. Additional data related to this paper may be requested from the authors. All data, theory details, simulation details, and experiment details presented in this work are available upon request to J.W.

Submitted 31 July 2018
Accepted 24 April 2019
Published 31 May 2019
10.1126/sciadv.aau9593

Citation: N. Zhou, S. Zheng, X. Cao, Y. Zhao, S. Gao, Y. Zhu, M. He, X. Cai, J. Wang, Ultra-compact broadband polarization diversity orbital angular momentum generator with 3.6 × 3.6 μm^2 footprint. *Sci. Adv.* **5**, eaau9593 (2019).